Crustal-scale listric geometry of the San Andreas Fault driven by lower crustal flow

Authors: Haibin Yang[1,2], Louis N. Moresi [2,1], Mark Quigley[1]

Affiliation 1: School of Earth Sciences, University of Melbourne, Victoria, Australia

Affiliation 2: Research School of Earth Science, Australian National University, Canberra, Australia

Corresponding Author: Haibin Yang

Email: haibiny@student.unimelb.edu.au

This is a non-peer reviewed preprint submitted to EarthArXiv.

13   **Abstract**

14   The San Andreas Fault (SAF) is one of the dominant components of the transform

15   boundary between the Pacific and the North American Plate. Although the fault is vertical-

16   to sub-vertical at shallow (<10 km) depth, it variably dips at angles of ca. 40-70º to the south-

17   west near the western Transverse Range and to the northeast in its southern segment at

18   depths of ca. 10-20 km, and thus can be described as having a listric geometry at the crustal

19   scale. The mechanism controlling the fault dip direction variation at depth along SAF is not

20   well understood. We utilize a 3D, finite element thermomechanical, viscoplastic model to

21   simulate lithospheric deformation associated with the SAF. The Big Bend of the fault near

22   the western Transverse Range is taken as a geometrical initial condition. Numerical exper-

23   iments demonstrate that regional lower crust strength variation along the SAF strike is an

24   important control on fault dip direction. For two blocks separated by transpressional faults,

25   viscous lower crustal material moves from the high viscosity (strong) block to the lower vis-

26   cosity (weak) lower crustal block. Fault-plane-normal flow in the viscous lower crust forces

27   fault dip direction at brittle-ductile transitional depth to rotate in the flow direction. Geophys-

28   ical data suggest that the Great Valley (eastern block) and south coast area (western block)

29   have stronger lower crust than their opposing fault blocks and that the SAF dips towards the

30   weaker block in both instances. Our self-consistent model also sheds light on the left-lateral

31   Garlock Fault, which intersects the right-lateral SAF in the western Transverse Range. To

32   maintain a vertical dip in the shallow crust and structural-kinematic connectivity with the

33   migrating fault zone at visco-elastic depths, the SAF may exhibit spatiotemporal transience

34   in upper crustal fault location and geometry over geological time scales, including strain

35   zone widening and dispersions. This behavior is expected to have ramifications for SAF

36   earthquake behaviors including rupture nucleation locations and segmentation and adds

complexity to expectations that strain should localize on sub-vertical strike-slip faults with increasing fault maturity.

1   Introduction

In a triaxial stress system with orthogonal principal compressive stresses $\sigma_1 > \sigma_2 > \sigma_3$, where σ_1 and σ_3 are horizontal and σ_2 is vertical, shear failure in intact rock is expected to occur on subvertical strike-slip faults oriented $\sim 30°$ to σ_1 (Anderson, 1905). With progressive deformation, formed faults may grow and interact (Roy and Royden, 2000b; Yang et al., 2020) and kinematically and geometrically evolve in ways that may be influenced by lithospheric conditions such as crustal rheology (Roy and Royden, 2000b, a), changes in the strain field (Koons et al., 2003), and other lithospheric conditions (Bowman et al., 2003; Yang et al., 2018). Optimally-oriented sub-vertical strike-slip faults could be expected to maintain steeply dipping geometries over geological time-scales. However, some of the largest plate boundary strike-slip faults on Earth, e.g., San Andreas Fault in California, Alpine Fault in New Zealand, Denali Fault in Alaska, have complicated geometries that include oppositely dipping and geometrically and kinematically distinct fault segments. The San Andreas Fault (SAF, Fig. 1) is a classical continental transform boundary between the Pacific and North American plates that accommodates 20-75 % of the relative motion between the two plates (~ 50 mm yr^{-1}) (Atwater and Stock, 1998; DeMets and Dixon, 1999; Meade and Hager, 2005) but varies in dip and geometry along strike and is thus a focus of this study.

Models for crustal deformation and earthquake rupture studies commonly simplify the SAF as a vertical or steeply dipping fault (Meade and Hager, 2005; Plesch et al., 2007). The

segment dipping ~50⁰-70⁰ northeast in the southern end of the SAF has been revealed by geodetic (Lindsey and Fialko, 2013), high-precision earthquake relocation (Lin et al., 2007) and seismic reflection studies (Fuis et al., 2017), while the segment near the Big Bend was found to dip 55⁰-75⁰ southwest by the analysis of potential-field data (Fig. 1) (Fuis et al., 2012). Recent earthquake hypocenter relocation studies show that the straight section to the north of the Big Bend is steeply dipping (Kim et al., 2016).

A non-vertical strike-slip fault plane may be an inherited structure from previous moderately dipping fabrics in mid-lower crustal depth (Schulte-Pelkum et al., 2020), or caused by transpressional deformations with a large ratio (>~0.4) of normal to transcurrent displacement that drives fault rotation (Braun and Beaumont, 1995). In a transpressional stress regime, the Anderson theory of faulting predicts conjugate fault planes, but it is hard to discern which one is the master fault. Roy and Royden (2000b) found the minor faults adjacent to the subvertical strike-slip fault plane might have moderately dipping angles at the brittle-ductile depth, but it cannot explain geometry of the major fault like the SAF. The static solution of Anderson faulting theory neglects the long-term evolution of a fault and the depth dependent rheology in crust.

We use the numerical geodynamic modelling method to simulate the long-term behavior of the SAF and propose that the deep ductile deformation due to viscosity contrast between two fault-bounded blocks would affect shallow, brittle-fault kinematics. To test our hypothesis, regional geophysical observations are combined to examine the ductile strength in the lithosphere. Modelling results also shed light on secondary fault distributions associated with SAF, e.g., the Garlock fault intersecting the SAF near the Big Bend (Fig. 1).

2   Methods

The particle-in-cell, finite-element, geodynamics code Underworld2 ([Mansour et al., 2020](https://doi.org/10.5281/zenodo.1436039)) is used to model the 3D thermo-mechanical deformation in the SAF system ([Moresi et al., 2007](#)). Underworld2 solves the equations for conservation of momentum and mass (incompressible material). The resulted velocity field are coupled in temperature calculation with advection-diffusion equation. The Boussinesq approximation is assumed for the equation of state.

We assume a power law dislocation creep to represent viscous flow. Drucker-Prager pressure-dependent yielding criteria is used for plastic deformation $\sigma_{yield} = Ptan\phi + C$, where σ_{yield} is the maximum second deviatoric stress invariant, $tan\phi$ is the friction coefficient and C is the cohesion. Linear strain weakening of the friction coefficient (0.4-0.02) and cohesion (20-5 MPa) between plastic strains of 0.5 and 1.5 allows for strain localization. Visco-plastic flow is modelled through an effective viscosity: $\eta_{vp} = min\left(\eta, \frac{\sigma_{yield}}{2\dot{\varepsilon}_{II}}\right)$, where η is the viscosity represented by power law dislocation creep, and $\dot{\varepsilon}_{II}$ is the second invariant of strain rate. The viscosity is limited in the range between 10^{19} Pa·s and 10^{24} Pa·s. Parameters used in the numerical experiments are listed in Table 1.

3   Model description

The model domain has total dimensions of 600 × 300 ×120 km with 144×72×48 linear, quadrilateral elements (Fig. 1). The 120-km-thick model consists of a 30-km-thick crust and a 90-km-thick mantle. Based on regional tectonic settings, the calculation domain is divided into 3 tectonic blocks: the coast area (west of SAF), the Great Valley (east of SAF and north

103 of the Garlock Fault), and the Sierra Nevada-Mojave (east of SAF) (Fig.1).Seismic surveys

104 show that the crustal thickness in the Coast Range (north of the coast area) to be 25-30 km

105 thick and 30-35 km in the other blocks (Mooney and Weaver, 1989; Jones et al., 1994;

106 Fliedner et al., 1996; Zhu and Kanamori, 2000). We set a constant value of 30 km for crustal

107 thickness and neglect lateral variations.

108   The crust is generally composed of felsic upper crust and mafic lower crust, but the

109 absence of mafic lower crust in the Mojave block is suggested by many seismic studies. A

110 Receiver function study found the Vp/Vs ratio < 1.75, indicating a felsic crust (Zhu and Kan-

111 amori, 2000). A seismic refraction survey (Fuis et al., 2001) detected the seismic P wave

112 velocity in lower crust to be 6.3 km/s. This is unusually low: mafic lower crust generally has

113 a P wave velocity of > 6.5 km/s. which might be caused by removing of mafic lower crust

114 which can be linked to surface magmatism dated to early Miocene (ca. 22-24 Ma) (Glazner

115 et al., 2002). The southeast Sierra Nevada is also thought lost its crustal root (Jones et al.,

116 1994; Fliedner et al., 1996), and the delamination is estimated to occur ca. 3.5 Ma, which is

117 evidenced by a pulsive emplacement of mafic potassic magmatism emplaced during 4-3 Ma

118 (Manley et al., 2000). Therefore, both the Mojave and Sierra Nevada block are designed in

119 our models to have no mafic lower crustal layer.

120   The model evolution time in our numerical experiments is < 4 Myr. Because the relative

121 motion direction between the North American plate and Pacific plate shows no significant

122 changes since 8 Ma (Atwater and Stock, 1998), the boundary conditions in our model do

123 not vary with model evolution. A constant shear velocity (V_x) of 40 mm yr^{-1} is applied on the

124 back plane (y = 300 km) while the velocity in the front plane (y = 0 km) is zero. Free slip

125 conditions are applied on the other boundaries. The initial condition for temperature field

126   assumes half-space cooling model at 50 Myr. The resulting temperature at the Moho depth

127   (30 km) is 550°C and surface heat flow is 50 mW m^{-2}.

128   The model includes a pre-defined weak zone with a Big Bend in the initial setup (Fig.

129   1). The 4-6 Ma near-fault block uplift of the San Emigdio Mountains along the Big Bend

130   indicated from low-temperature thermochronology studies (Niemi et al., 2013) may be at-

131   tributed to the intensive transpressional strain near the Big Bend. In this case, we assume

132   that the Big Bend has formed when the model begins, though the exact time or mechanism

133   for the formation of Big Bend is debated (Popov et al., 2012; Niemi et al., 2013). The weak

134   zone is initially represented by materials with plastic strain of 2, which is the upper limit of

135   the linear strain weakening, and the corresponding effective cohesion and friction coefficient

136   are 5 MPa and 0.02, respectively. This produces a weak fault as observed in regional stress

137   mapping and laboratory experiments (Zoback et al., 1987; Collettini et al., 2009; Lockner et

138   al., 2011). The fault plane is assumed to be vertical everywhere along the fault strike but

139   can deform with time. Fault is set to cut into 60 km deep to the mantle. A 50-km-wide and

140   60-km-deep buffer zone is added to both ends of SAF to minimize artificial boundary effects.

141   The buffer zone has a relatively weak viscosity of 10^{20} Pa·s; this value is applied to all ma-

142   terial particles that enter the buffer zone.

143

144   **4   Results**

145   A successful model should produce along-strike variations of the fault dipping direction

146   that are comparable with those detected in SAF, and other more features agree with obser-

147   vations in the SAF system. We have run series of models to test the influence of lower crust

148 rheology and its heterogeneity distribution related to the composition or temperature heter-

149 ogeneities. Here we show three main models: Model 1, Model 2, and Model 3. The crust in

150 Model 1 has only one layer (the whole crust in all blocks is represented by quartzite rheol-

151 ogy). With all other parameters being equal, Model 2 has a mafic lower crust in the Great

152 Valley (20 km thick) and coast area (15 km thick). Model 1 and Model 2 show different

153 deformation patterns after 2 Myr evolution. In Model 2, the fault plane of the southern end

154 (x = 350 - 500 km) evolves from initially vertical to dipping towards the Mojave block at ~60

155 ° (Fig. 2a & 2b). No moderately dipping fault as Model 2 form in Model 1. Moreover, a shear

156 band along the southern boundary of the Great Valley block occurs in Model 2 rather than

157 Model 1 (Fig. 2a and 2b).

158   For Model 2, replacing the two-layered crust in Great Valley with only one layer of

159 quartzite rheology does not change the dipping pattern of Model 2, but a strong lower crust

160 in the coast area is required to form a dipping fault toward the Mojave block. With these

161 observations, the corollary is that lower crust viscosity contrast (>10^2 Pa•s) between two

162 fault-separated blocks appears to determine the fault dip direction. We found that the strong

163 lower crust material flows to the other fault-bounded block that has a weaker lower crust. In

164 turn, the lower part of the upper crust overlying a weak lower crust thrust on top the footwall

165 that has a strong lower crust. In this scenario, the fault dip direction is in accord with the

166 relative motion between lower crust material across the fault.

167   Model 2 only produces the fault that is dipping to the Mojave block, and no dip direction

168 variation along the strike. Model 3 is adapted from Model 2 and reduces mafic lower crust

169 thickness in the central coast area (x = 250 - 400 km) from 15 km to 5 km (Fig. 1). Moreover,

170 to reflect lateral temperature heterogeneities in lithosphere, the initial temperature in the

coast area follows the 30 Myr oceanic lithosphere geotherms, and that in Mojave block linearly increases from 30 Myr at the west boundary (the Big Bend) to 40 Myr at the east boundary (y = 200 km), beyond which the temperature follows the 40-Myr oceanic lithosphere geotherm. The Great Valley keeps 50 Myr geotherms.

The model (Fig.2c) shows that formation of a shear band near the southmost edge of the Great Valley as in Model 2. The northeast-dipping fault appears at the southern SAF (x > 430 km) while the fault near the Bid Bend (250 km < x < 320 km) dips towards the coast area. In-between the northeast and southwest dipping fault segment (x=320 – 430 km), there is a segment of nearly vertical fault plane (Fig. 2c). This is comparable with the first order features of fault dipping pattern in the SAF in the Southern California (Fig. 1).

5 Discussion

The numerical models indicate that lower crustal rheology controls the brittle fault dip direction in the setting like the SAF. In the following sections, comprehensive geophysical observations are utilized to infer the in-situ lower crustal rheology in the SAF system.

5.1 Rheology variation along the SAF

Model 3 requires higher viscosity of lower crust in the Great Valley than that in the central coast area (the Western Transverse Range), and the viscosity in the south coast range (west to the SAF) is higher than that in Mojave block (close to the San Bernardino Mountains). The seismogenic layer thickness in the crust may reflect the strength of the crust, which is a combination of the effects of temperature, composition, and strain rate. Generally, the thicker the seismogenic layer, the stronger (higher viscosity) the lower crust may be. Regional relocated Earthquakes from the Southern California Earthquake Data

193   Center are used to calculate the seismogenic thickness (Hauksson et al., 2012). The re-

194   ported hypocenter depth uncertainty is less than 1.25 km at 90% confidence. We draw three

195   profiles (P1, P2 and P3 in Fig.1) of 60 km long across the different segments of the SAF.

196   The SAF is in the midpoint of each profile. Earthquakes within 20 km of the selected line are

197   projected to the corresponding profile. For each half section, the seismogenic thickness is

198   defined as a depth above which 95% of the events are located and marked as D95 (Fig. 3).

199   The P1 and P3 profiles sample the earthquakes in the SAF segment with moderate dip

200   and show D95 differences between the fault-bounded blocks of more than 5 km (Fig. 3). In

201   contrast, P2 profile located in the near-vertical segment demonstrates that the contrast of

202   D95 depth for two blocks is less than 1 km (Fig. 3). Additionally, the D95 in the Great Valley

203   (20.0 km) is deeper than that to the west (14.3 km), and the D95 in the San Bernardino

204   Mountains (13.0 km) is shallower than that to the west of the SAF (18.2 km). This indicates

205   stronger lower crust in the Great Valley than that in the Western Transvers Range, and that

206   the San Bernardino Mountains may have lower viscosity in the deep crust than the block to

207   the west of the SAF. This is consistent with the rheology requirement in the numerical model

208   to cause the southwest-dipping fault near the Big Bend and northeast-dipping fault to the

209   southmost segment.

210   Topographic swaths 40 km wide along each of the three sections are compiled to see

211   whether the strain asymmetry is reflected in topography. The asymmetry of seismogenic

212   thickness distribution across the SAF in P1 and P3 is seen in the topography as well (Fig.

213   3). For the median lines in P1 and P3, the block of deeper D95 has about 1500 m lower

214   elevation than the one of thinner seismogenic thickness, and the P2 profile shows the dif-

215   ference in topography is less than 500 m (Fig. 3). The topography difference is potentially a

216   reflection of regional crustal thickness and density variation. We further collect the density

217   information in the crystalline crust which is derived from the inversion of residual gravity

218   anomaly that has the influence of sediments and variations in Moho depth removed (Kaban

219   and Mooney, 2001). They found that the density in the Great Valley (3000-3100 kg/m^3) is

220   much higher than that in the Western Transverse Range (<3000 kg/m^3) for the Big Bend

221   area. Since the inversion method only considers anomalies of wavelength larger than 150

222   km, the horizontal resolution is too limited to distinguish between P2 and P3. For the south-

223   ern SAF, the first-order observation is that the density in the block located west of SAF (coast

224   side) is about 50 kg/m^3 higher than that in the east block (Mojave side). The density in crys-

225   talline crust is a good indicator of bulk crust composition, i.e., higher densities correspond

226   to rheologically stronger, quartz-poor compositions. The high density in the Great Valley has

227   been interpreted to be oceanic in nature, composed of mafic and ultra-mafic rocks (Kaban

228   and Mooney, 2001). The Great Valley functions as a rigid block and almost accommodates

229   no deformation in its interior, as is seen from surface slip field recorded by GPS observations

230   (Shen-Tu et al., 1999; Tong et al., 2014).

231   Although material of higher seismic wave velocity does not always correspond to higher

232   viscosity, seismic wave velocity tomography at the comparable depths beneath surface is

233   thought to be a good proxy of strength (viscosity) contrast in the lower crust. High-resolution

234   S wave tomography shows that, at depth of 20 km, the Great Valley and the south coast

235   area has high shear velocity (4.0-4.2 km/s) in the region. The corresponding upper plate

236   (i.e., the hanging wall of the transpressional fault), the Western Transverse Range and south

237   Mojave, have the low velocity (3.4-3.8 km/s) in the region. The vertical segment that lies in-

238   between, both sides of the fault are of low velocity (3.4-3.8 km/s) (Lee et al., 2014). The first

239   order features of S wave velocity are also mapped by other seismic studies (Tape et al.,

240   2009; Tape et al., 2010; Lee and Chen, 2017). Both the gravity and seismic surveys support

241 a stronger lower crust in the Great Valley and the south coast area than in the Western

242 Transverse Range and the San Bernardino Mountains, respectively. Such rheology contrast

243 may form the moderately dipping fault in the transpressional environment as observed in

244 our numerical models.

245   The moderately dipping segment at the southern end was suggested to root in shallowly

246 dipping fabrics in the ductile lower crust which was revealed by seismic anisotropic studies

247 (Schulte-Pelkum et al., 2020). This observation does not conflict with our hypothesis. The

248 inherited layered weak zones at the brittle-ductile transitional depth can be a sharp boundary

249 to facilitate the fault-normal movement at the brittle-ductile transitional depth. On the other

250 hand, the seismic anisotropic features can be attributed to or enhanced by the fault-normal

251 movement at the brittle-ductile transitional depth in the Southern California.

252 **5.2   Depth distribution of earthquakes in Southern California**

253   We compare the depth variation of earthquake occurrence for four areas in Southern

254 California. Two regions are along the SAF, one close to the Big Bend (Bend in Fig. 4) and

255 the other to the west of the southern SAF (WSAF in Fig. 4). The other two are in the Eastern

256 California Shear zone, one north to the Garlock Fault (NGF in Fig. 4) and the other south to

257 the Garlock Fault (SGF in Fig. 4). With the focal mechanism solution data from Southern

258 California Earthquake Data Center (Yang et al., 2012), we select events with magnitude >

259 1, and divide them in to two groups: one has shallow dip (< 30°) and the other steep dip (>

260 80°). The total events are also plotted as a reference.

261   The total cases and the steep group have a consistent trend of depth distribution, i.e.,

262 the peak number of occurrence frequency occurs at depth of 2-10 km, after which it de-

263 creases with depth (Fig. 4). The shallow dip group shows the same trend for those in the

264   Eastern California Shear Zone (NGF and SGF in Fig. 4), but different features for those

265   along the SAF where there are moderately dipping fault planes. The maximum in the SAF

266   cases (Bend and WSAF in Fig. 4) occurs at the depth to the base of the seismogenic layer.

267   We note that the total number of earthquakes in the Bend is less than the number of those

268   occurring in SGF, but the number of earthquakes in the shallow group for the Bend at depth >

269   10 km is still larger than that in SGF. That means the shallow cases in the moderately dipping

270   segments of SAF is statistically significant and is not biased by total numbers. The depth

271   variation of earthquakes with steep and shallow dips suggests that the selected seismogenic

272   faults are steeply dipping at depth < 10 km but may gradually reduce their dip at depth for

273   those in the SAF. This is consistent with the seismic image of the southern SAF near the

274   Salton Sea, which is detected to be near vertical at shallow depth (<9 km), but dips ~50° –

275   60° northeast for the deeper part (Fuis et al., 2017). This pattern is also found in our numer-

276   ical models: the deeper part (>10 km) is affected by the long-term ductile transpressional

277   deformation, which is initially set to be vertical (Fig. 5). The shallow groups at deeper part in

278   the young fault zone, NGF and SGF, is not as significant as that in the SAF, which is con-

279   sidered as a mature fault that has evolved for 10's million years. The long-term evolution of

280   the SAF might have been subjected to fault-plane-normal shear stress imparted from the

281   viscous flow moving from the fault-bounded block with high viscosity to the one with low

282   viscosity in a transpressional stress regime. Such fault-plane-normal flow in the lower crust

283   could have forced the fault dip at the brittle-ductile depth to the flow direction.

284   **5.3   Garlock Fault**

285   Our numerical experiments predict formation of a major shear band along the southern

286   boundary of the Great Valley block. The shear band mimics the Garlock fault that intersects

287   the SAF near the Big Bend and may explain its activity. Formation of the Garlock fault is

288   debated with three broadly proposed models: (1) extrusion as a conjugate fault of the SAF

289   (Hill and Dibblee, 1953), (2) transform fault for the Basin and Range extension (Davis and

290   Burchfiel, 1973), (3) rotation of the Mojave block (Guest et al., 2003). Our model suggests

291   that formation of the Garlock fault requires a stronger lower crust in the coast area than the

292   Mojave block (Fig. 5). This has consistent with both gravity and seismic observations (Kaban

293   and Mooney, 2001; Lee et al., 2014). As the strong Great Valley block moves towards the

294   Mojave block, it is impeded by strong coast area, squeezing out the Mojave block. This is

295   accommodated by the leftlateral Garlock fault (Fig. 2 & 5). The Garlock fault was thought to

296   begin its sinistral slip ca. 11 Ma (Andrew et al., 2014), and the eastern branch of the Garlock

297   fault might have been related to extension of the Basin and Range and the East California

298   Shear Zone development (Davis and Burchfiel, 1973; Hatem and Dolan, 2018), the effect of

299   which is not considered in our numerical model. Our model supports the extrusion model for

300   the western branch of the Garlock fault. On the other hand, our model suggests the Basin

301   and Range extensions that have weakened the lithospheric strength may be an important

302   'open' boundary to facilitate the extrusion of the Mojave block.

303   **6   Conclusions**

304   This study focuses on the formation of moderately dipping fault segments of the strike-slip

305   San Andreas fault. 3D numerical models suggest the lower crustal viscosity contrast across

306   the fault plane might have controlled the fault dip direction in a transpressional environment.

307   The fault-normal flow direction in the viscous lower crust near the strike-slip fault plane is

308   from the one with higher viscosity to the one with lower viscosity. The long-term viscous

309   deformation upward reduces the dip angle of the initially near vertical fault plane at the brit-

310   tle-ductile transition depth. This is consistent with the observations of the moderately dipping

311 segments of the San Andreas fault: a near-vertical fault plane for shallow depth (< 10 km),

312 and a shallow dip angle at depth > 10km. The viscosity contrast across the fault plane is

313 consistent with seismogenic thickness variations along the San Andreas fault, and other

314 geophysical observations.

315

323 **References**

324 Anderson, E., 1905. The dynamics of faulting. Transactions of the Edinburgh

325 Geological Society 8, 387-402.

326 Andrew, J.E., Walker, J.D., Monastero, F.C., 2014. Evolution of the central Garlock

327 fault zone, California: A major sinistral fault embedded in a dextral plate margin. Geological

328 Society of America Bulletin, B31027. 31021.

329 Atwater, T., Stock, J., 1998. Pacific-North America plate tectonics of the Neogene

330 southwestern United States: an update. International Geology Review 40, 375-402.

331   Bowman, D., King, G., Tapponnier, P., 2003. Slip partitioning by elastoplastic

332   propagation of oblique slip at depth. Science 300, 1121-1123.

333   Braun, J., Beaumont, C., 1995. Three‐dimensional numerical experiments of strain

334   partitioning at oblique plate boundaries: Implications for contrasting tectonic styles in the

335   southern Coast Ranges, California, and central South Island, New Zealand. Journal of

336   Geophysical Research: Solid Earth 100, 18059-18074.

337   Collettini, C., Niemeijer, A., Viti, C., Marone, C., 2009. Fault zone fabric and fault

338   weakness. Nature 462, 907-910.

339   Davis, G.A., Burchfiel, B.C., 1973. Garlock fault: An intracontinental transform structure,

340   southern California. Geological Society of America Bulletin 84, 1407-1422.

341   DeMets, C., Dixon, T.H., 1999. New kinematic models for Pacific-North America motion

342   from 3 Ma to present, I: Evidence for steady motion and biases in the NUVEL-1A model.

343   Geophysical Research Letters 26, 1921-1924.

344   Fliedner, M.M., Ruppert, S., Malin, P.E., Park, S.K., Jiracek, G., Phinney, R.A., Saleeby,

345   J.B., Wernicke, B., Clayton, R., Keller, R., Miller, K., Jones, C., Luetgert, J.H., Mooney, W.D.,

346   Oliver, H., Klemperer, S.L., Thompson, G.A., 1996. Three-dimensional crustal structure of

347   the southern Sierra Nevada from seismic fan profiles and gravity modeling. Geology 24,

348   367-370.

349   Fuis, G.S., Bauer, K., Goldman, M.R., Ryberg, T., Langenheim, V.E., Scheirer, D.S.,

350   Rymer, M.J., Stock, J.M., Hole, J.A., Catchings, R.D., 2017. Subsurface Geometry of the

351   San Andreas Fault in Southern California: Results from the Salton Seismic Imaging Project

352   (SSIP) and Strong Ground Motion Expectations. Bulletin of the Seismological Society of

353   America.

354   Fuis, G.S., Ryberg, T., Godfrey, N.J., Okaya, D.A., Murphy, J.M., 2001. Crustal

355   structure and tectonics from the Los Angeles basin to the Mojave Desert, southern California.

356   Geology 29, 15-18.

357   Fuis, G.S., Scheirer, D.S., Langenheim, V.E., Kohler, M.D., 2012. A New Perspective

358   on the Geometry of the San Andreas Fault in Southern California and Its Relationship to

359   Lithospheric Structure. Bulletin of the Seismological Society of America 102, 236-251.

360   Glazner, A.F., Walker, J.D., Bartley, J.M., Fletcher, J.M., 2002. Cenozoic evolution of

361   the Mojave block of southern California. Geologic evolution of the Mojave Desert and

362   southwestern Basin and Range: Geological Society of America Memoir 195, 19-41.

363   Guest, B., Pavlis, T.L., Golding, H., Serpa, L., 2003. Chasing the Garlock: A study of

364   tectonic response to vertical axis rotation. Geology 31, 553-556.

365   Hatem, A.E., Dolan, J.F., 2018. A model for the initiation, evolution, and controls on

366   seismic behavior of the Garlock fault, California. Geochemistry, Geophysics, Geosystems.

367 Hauksson, E., Yang, W.Z., Shearer, P.M., 2012. Waveform Relocated Earthquake

368 Catalog for Southern California (1981 to June 2011). Bulletin of the Seismological Society

369 of America 102, 2239-2244.

370 Hill, M.L., Dibblee, T.W., 1953. San Andreas, Garlock, and Big Pine Faults, California

371 - a Study of the Character, History, and Tectonic Significance of Their Displacements.

372 Geological Society of America Bulletin 64, 443-&.

373 Jones, C.H., Kanamori, H., Roecker, S.W., 1994. Missing roots and mantle "drips":

374 Regional Pn and teleseismic arrival times in the southern Sierra Nevada and vicinity,

375 California. Journal of Geophysical Research: Solid Earth 99, 4567-4601.

376 Kaban, M.K., Mooney, W.D., 2001. Density structure of the lithosphere in the

377 southwestern United States and its tectonic significance. J Geophys Res-Sol Ea 106, 721-

378 739.

379 Karato, S.I., Jung, H., 2003. Effects of pressure on high-temperature dislocation creep

380 in olivine. Philosophical Magazine 83, 401-414.

381 Kim, W., Hong, T.K., Lee, J., Taira, T., 2016. Seismicity and fault geometry of the San

382 Andreas fault around Parkfield, California and their implications. Tectonophysics 677, 34-

383 44.

384   Koons, P.O., Norris, R.J., Craw, D., Cooper, A.F., 2003. Influence of exhumation on

385   the structural evolution of transpressional plate boundaries: An example from the Southern

386   Alps, New Zealand. Geology 31, 3-6.

387   Lee, E.J., Chen, P., 2017. Subsurface fault geometries in Southern California

388   illuminated through Full-3D Seismic Waveform Tomography (F3DT). Tectonophysics 703,

389   42-49.

390   Lee, E.J., Chen, P., Jordan, T.H., Maechling, P.B., Denolle, M.A.M., Beroza, G.C.,

391   2014. Full-3-D tomography for crustal structure in Southern California based on the

392   scattering-integral and the adjoint-wavefield methods. J Geophys Res-Sol Ea 119, 6421-

393   6451.

394   Lin, G.Q., Shearer, P.M., Hauksson, E., 2007. Applying a three-dimensional velocity

395   model, waveform cross correlation, and cluster analysis to locate southern California

396   seismicity from 1981 to 2005. J Geophys Res-Sol Ea 112.

397   Lindsey, E.O., Fialko, Y., 2013. Geodetic slip rates in the southern San Andreas Fault

398   system: Effects of elastic heterogeneity and fault geometry. J Geophys Res-Sol Ea 118,

399   689-697.

400   Lockner, D.A., Morrow, C., Moore, D., Hickman, S., 2011. Low strength of deep San

401   Andreas fault gouge from SAFOD core. Nature 472, 82-85.

402   Manley, C.R., Glazner, A.F., Farmer, G.L., 2000. Timing of volcanism in the Sierra

403   Nevada of California: Evidence for Pliocene delamination of the batholithic root? Geology

404   28, 811-814.

405   Mansour, J., Giordani, J., Moresi, L., Beucher, R., Kaluza, O., Velic, M., Farrington,

406   R.J., Quenette, S., Beall, A.P., 2020. Underworld2: Python geodynamics modelling for

407   desktop, hpc and cloud. Journal of Open Source Software 5, 1797.

408   Meade, B.J., Hager, B.H., 2005. Block models of crustal motion in southern California

409   constrained by GPS measurements. J Geophys Res-Sol Ea 110.

410   Mooney, W.D., Weaver, C.S., 1989. Regional crustal structure and tectonics of the

411   Pacific coastal states; California, Oregon, and Washington. Geological Society of America

412   Memoirs 172, 129-162.

413   Moresi, L., Quenette, S., Lemiale, V., Meriaux, C., Appelbe, B., Mühlhaus, H.-B., 2007.

414   Computational approaches to studying non-linear dynamics of the crust and mantle. Physics

415   of the Earth and Planetary Interiors 163, 69-82.

416   Niemi, N.A., Buscher, J.T., Spotila, J.A., House, M.A., Kelley, S.A., 2013. Insights from

417   low-temperature thermochronometry into transpressional deformation and crustal

418   exhumation along the San Andreas fault in the western Transverse Ranges, California.

419   Tectonics 32, 1602-1622.

420   Plesch, A., Shaw, J.H., Benson, C., Bryant, W.A., Carena, S., Cooke, M., Dolan, J.,

421   Fuis, G., Gath, E., Grant, L., Hauksson, E., Jordan, T., Kamerling, M., Legg, M., Lindvall, S.,

422   Magistrale, H., Nicholson, C., Niemi, N., Oskin, M., Perry, S., Planansky, G., Rockwell, T.,

423   Shearer, P., Sorlien, C., Suss, M.P., Suppe, J., Treiman, J., Yeats, R., 2007. Community

424   fault model (CFM) for southern California. Bulletin of the Seismological Society of America

425   97, 1793-1802.

426   Popov, A.A., Sobolev, S.V., Zoback, M.D., 2012. Modeling evolution of the San

427   Andreas Fault system in northern and central California. Geochem Geophy Geosy 13, n/a-

428   n/a.

429   Ranalli, G., 1995. Rheology of the Earth. Springer Science & Business Media.

430   Roy, M., Royden, L.H., 2000a. Crustal rheology and faulting at strike‐slip plate

431   boundaries: 1. An analytic model. Journal of Geophysical Research: Solid Earth 105, 5583-

432   5597.

433   Roy, M., Royden, L.H., 2000b. Crustal rheology and faulting at strike‐slip plate

434   boundaries: 2. Effects of lower crustal flow. Journal of Geophysical Research: Solid Earth

435   105, 5599-5613.

436   Schulte-Pelkum, V., Ross, Z.E., Mueller, K., Ben-Zion, Y., 2020. Tectonic Inheritance

437   With Dipping Faults and Deformation Fabric in the Brittle and Ductile Southern California

438   Crust. J Geophys Res-Sol Ea 125, e2020JB019525.

439   Shen-Tu, B.M., Holt, W.E., Haines, A.J., 1999. Deformation kinematics in the western

440   United States determined from Quaternary fault slip rates and recent geodetic data. J

441   Geophys Res-Sol Ea 104, 28927-28955.

442   Tape, C., Liu, Q., Maggi, A., Tromp, J., 2009. Adjoint tomography of the southern

443   California crust. Science 325, 988-992.

444   Tape, C., Liu, Q.Y., Maggi, A., Tromp, J., 2010. Seismic tomography of the southern

445   California crust based on spectral-element and adjoint methods. Geophysical Journal

446   International 180, 433-462.

447   Tong, X.P., Smith‐Konter, B., Sandwell, D.T., 2014. Is there a discrepancy between

448   geological and geodetic slip rates along the San Andreas Fault system? Journal of

449   Geophysical Research: Solid Earth 119, 2518-2538.

450   Wessel, P., Smith, W., Scharroo, R., Luis, J., Wobbe, F., 2013. Generic mapping tools:

451   improved version released. Eos, Transactions American Geophysical Union 94, 409-410.

452   Yang, H., Chemia, Z., Artemieva, I.M., Thybo, H., 2018. Control on off-rift magmatism:

453   A case study of the Baikal Rift Zone. Earth and Planetary Science Letters 482, 501-509.

454   Yang, H.B., Moresi, L.N., Quigley, M., 2020. Fault spacing in continental strike-slip

455   shear zones. Earth and Planetary Science Letters 530, 115906.

456   Yang, W., Hauksson, E., Shearer, P.M., 2012. Computing a large refined catalog of

457   focal mechanisms for southern California (1981–2010): Temporal stability of the style of

458   faulting. Bulletin of the Seismological Society of America 102, 1179-1194.

459   Zhu, L.P., Kanamori, H., 2000. Moho depth variation in southern California from

460   teleseismic receiver functions. J Geophys Res-Sol Ea 105, 2969-2980.

461   Zoback, M.D., Zoback, M.L., Mount, V.S., Suppe, J., Eaton, J.P., Healy, J.H.,

462   Oppenheimer, D., Reasenberg, P., Jones, L., Raleigh, C.B., Wong, I.G., Scotti, O.,

463   Wentworth, C., 1987. New evidence on the state of stress of the san andreas fault system.

464   Science 238, 1105-1111.

465

466

Figures

468
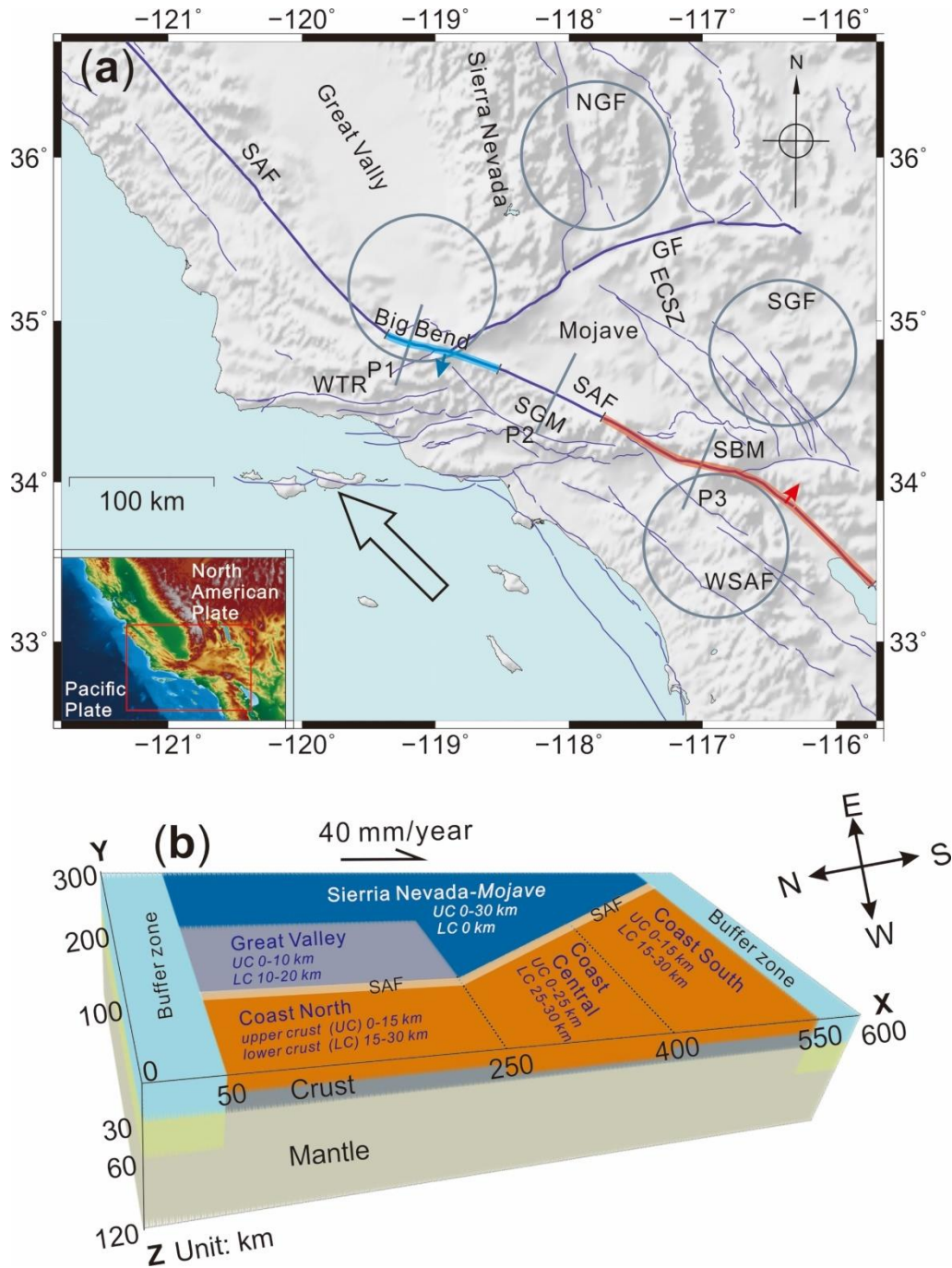
469 **Figure 1.** Tectonic settings of the San Andreas Fault system (a) and the simplified numerical

470 model setup (b). (a) Major faults (thick purple lines) including the San Andreas fault (SAF)

471 and the Garlock fault (GF) and other sub-major faults (thin purple lines) are marked on

472 shaded relief map. The arrow shows relative motion between the Pacific Plate and the North

473 American Plate. Along the SAF, the southwest dipping fault segment near the Big Bend is

474 coded as blue color while the northeast dipping segment in the southern end is denoted by

475 red color. Abbreviations for some main structures: SGM, San Gabriel mountain; SBM, San

476 Bernardino mountain; ECSZ, Eastern California Shear zone. WTR, Western Transverse

477 Range. The position of three profiles, P1, P2 and P3, shown in Figure 3 is marked by grey

478 lines. Four grey circles with a radius of 50 km show the area of the sampled earthquakes in

479 Figure 4. (b) The corresponding three-dimensional structure for the Model 3, and the details

480 of other models are stated in the context when used. The constant velocity 40 mm yr^{-1} to-

481 wards the positive x direction is applied on the back vertical plane (y = 300 km) while the

482 velocity in x direction in the front vertical plane (y = 0 km) is zero. Materials are not allowed

483 to move out/in the box, and free slip is applied for other velocity components.

484

485
486
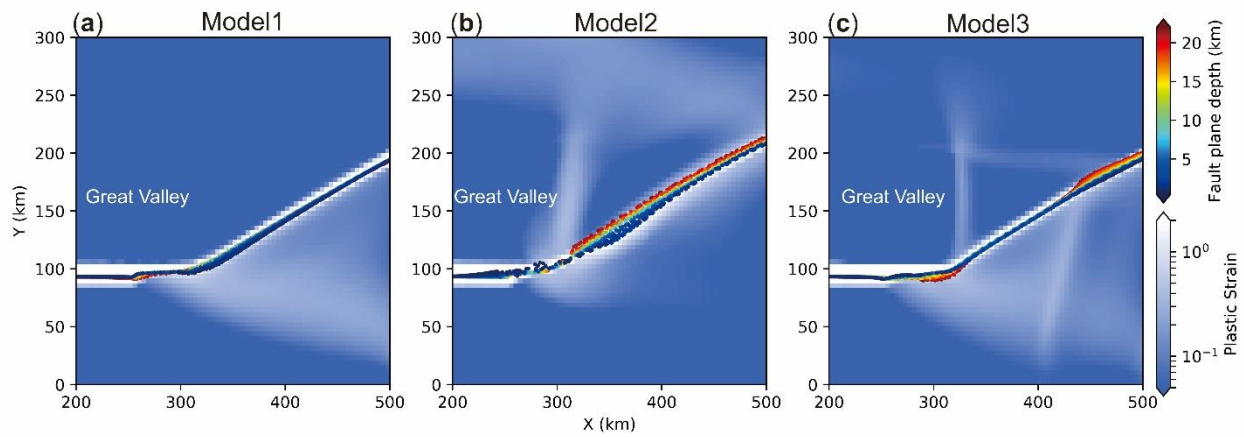
Figure 2. Snapshots of plastic strain distribution at depth of 5 km and the fault plane depth distribution after models running 2.1 Myr for Model 1 (a), Model 2 (b) and Model 3 (c), respectively. Localized shear bends along the right edge of the Great Valley happen to the Model 2 and Model 3. The initially vertical fault planes in Model 2 and Model 3 evolve to be at a moderately dip (~60º), while the Model 1 of a homogenous crustal property keeps the nearly vertical fault plane. The Model 3 with lateral viscosity variations in the lower crust produces the comparable features of the fault dipping direction variation along the SAF.

498 .
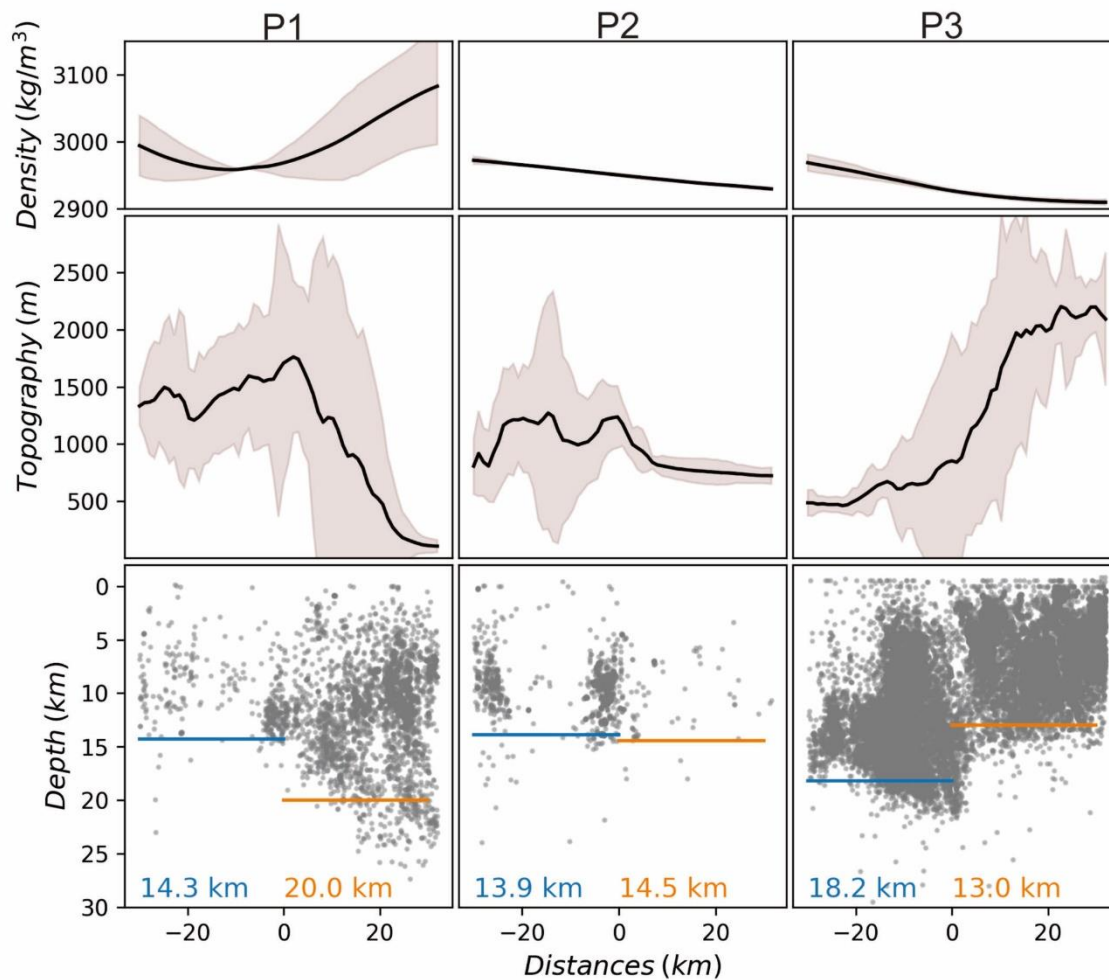
Figure 3. The density of the crystalline basement layer (upper panel), topography of
the earth surface (middle panel) and the earthquake depths (lower panel) distributions
along three profiles, P1, P2 and P3 (position marked in Figure 1). All these properties
are projected from distances < 20 km to the corresponding profile. The light red color
patches for density and topography show the envelope of the data range, and the black
line is the median value. The lines in lower panel marks the D95 depth, above which
95% of the earthquakes are located, for either block that is separated by the fault. The

506   SAF is located at the mid-point of the profile (distance = 0); all profiles start from south

507   with negative coordinates.

508
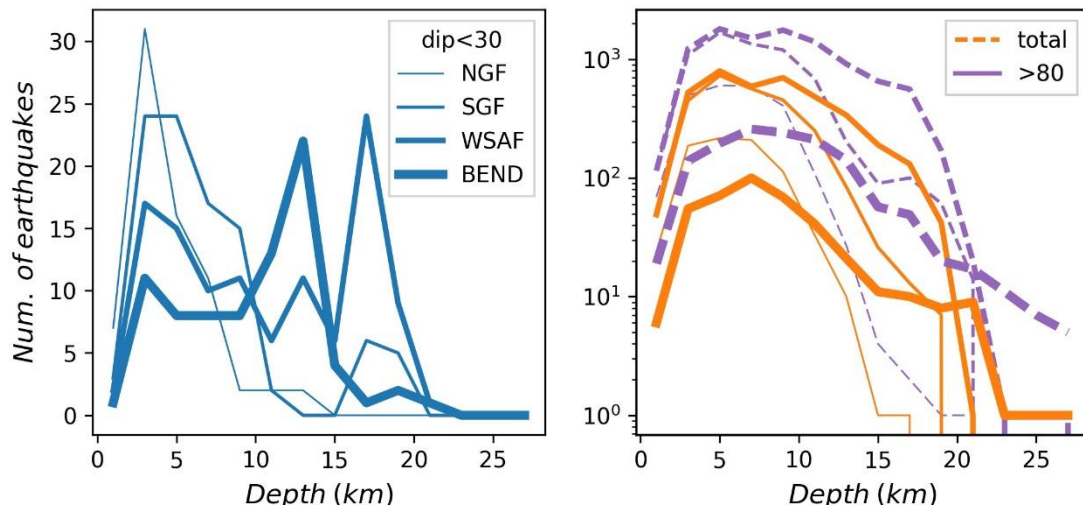
Figure 4. The depth distribution earthquakes in four areas (marked as circles in Figure 1). The NGF and SGF are sampled from north and south of the Garlock fault, respectively. The WSAF is located west of the SAF and BEND is closed to the Big Bend. The events are divided into two group: steep dip (> 80°) and shallow dip (< 30°), and the total events are also plot as a reference. The steep group shows the peak numbers of earthquakes appear at depth of 2 -10 km, but this trend in shallow group is only true for those in NGF and SGF. For the shallow group, the peak number in WSAF and BEND appears at the base of the seismogenic layers (12 - 20 km)

518
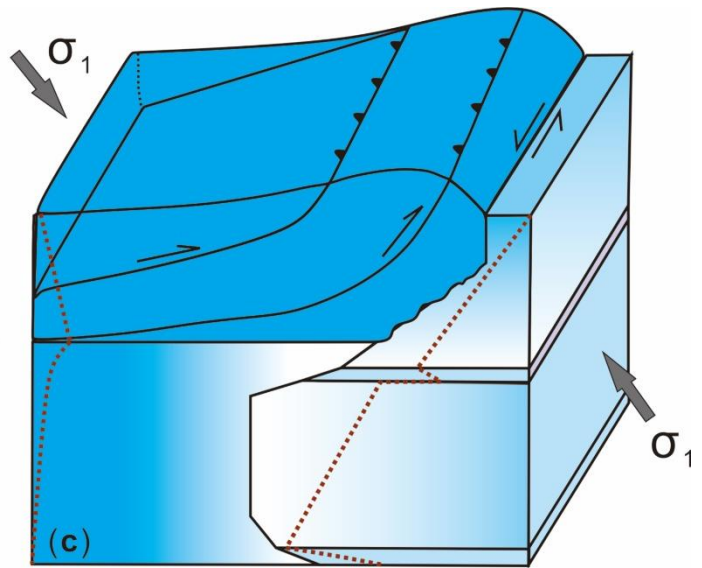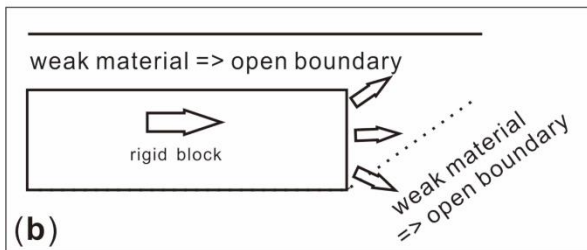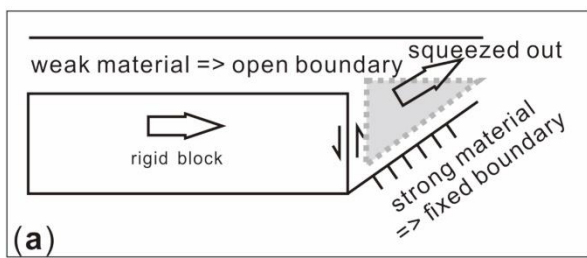
Figure 5. Sketch model describing how the lower crustal strength distribution affects re-

gional structure development. (a) A strong lower crust in the coast area of the Southern

California impedes the Mojave block moving southwest, and the Garlock Fault is formed to

accommodate the eastward escape of the Mojave block. (b) A weak lower crust in the coast

area tends to produce a diffusive deformation at the right edge of the Great Valley. (c) In a

transpressional environment, strong viscous lower crust tends to wedge into the weaker one

while the upper crust overlying a weak lower crust over thrust to the one with strong lower

crust. Therefore, the deep part of the originally vertical fault plane gradually evolves to be a

moderately dipping fault plane, the direction of which is consistent with the flow direction in

the lower crust. The red dashed lines stand for scaled strength profile of corresponding block.

530

531 **Tables**

532 **Table 1.** Model parameters：The power law dislocation creep is in viscous regime is described as

533 $\dot{\varepsilon} = A\sigma^n \exp\left(-\frac{E+VP}{RT}\right)$ where $\dot{\varepsilon}$ is strain rate, A material constant, σ deviatoric stress, n stress ex-

534 ponent, E activation energy, V activation volume, R the gas constant, and T temperature. The ef-

535 fective ductile viscosity $\eta = \frac{\sigma_{II}}{2\dot{\varepsilon}_{II}}$, where subscript marks the second invariant. Density $\rho = \rho_o[1 - $

536 $\alpha(T - T_0)]$, ρ_0 is the standard density at $P_O = 0.1$ MPa and $T_0 = 273$ K; Cp is heat capacity. α is

537 thermal expansion. k is heat conductivity, and H_r radioactive heat production.

	Upper crust[1]	Lower crust[1]	Mantle[2]
A (MPa^{-n} S^{-1})	3.2×10^{-4}	3.3×10^{-4}	1.3×10^{6}
n	2.3	3.2	3.0
E kJ/mol	154	240	510
V (cm^3/mol)	0	0	14
ρ_o (kg/m^3)	2700	2900	3300
Cp (J/kg)	1200	1200	1200
α (K^{-1})	3×10^{-5}	3×10^{-5}	3×10^{-5}
k(W/mK)[3]	2.5	3	3.5
H_r(μW/m^3)	2	0.1	0.01

538 [1] Ranalli (1995); [2] Karato and Jung (2003).

539